nature communications

Article

https://doi.org/10.1038/s41467-025-65652-9

Tricritical Kibble-Zurek scaling in Rydberg atom ladders

Received: 30 June 2025

Accepted: 21 October 2025

Published online: 26 November 2025

Check for updates

Hanteng Wang, Xingyu Li & Chengshu Li

The Kibble–Zurek (KZ) mechanism has been extensively studied in various second-order phase transitions, yet the case of tricriticality—the point where second-order phase transition lines terminate—remains experimentally elusive. Here, we theoretically propose probing KZ scaling at tricritical points using Rydberg atom arrays arranged as two- and three-leg ladders, which realize the tricritical Ising and tricritical Potts universality classes. By slowly ramping the Rabi frequency and detuning, we extract two relevant tricritical exponents, ν and ν', both via conventional paths from the disordered to the ordered phase and via "tangential" paths confined entirely within the disordered phase. At faster speeds, ramping dynamics go beyond the standard KZ paradigm: data collapse analysis using the parent critical exponents (rather than the tricritical ones) reveals renormalization group flows toward the adjacent second-order critical line, and we identify it as a dynamical analog of Zamolodchikov's c-theorem. Our protocol is readily implementable on existing Rydberg quantum simulators. This provides a direct route to measuring distinct tricritical exponents which can reveal an emergent spacetime supersymmetry constraint $1/\nu - 1/\nu' = 1$. Moreover, this work deepens our theoretical understanding and opens new avenues for exploring beyond-KZ quantum dynamics with rich renormalization group structure.

The Kibble–Zurek (KZ) mechanism concerns dynamical scaling behavior near a critical point[1,2]. Originally proposed in the context of classical phase transitions, its quantum counterpart has been extensively explored both within[3–11] and beyond[12–17] the Landau–Ginzburg–Wilson paradigm. With recent advances in quantum simulators, numerous experimental studies on artificial quantum platforms, such as superconducting qubits[18,19], ion traps[20–22], and Rydberg atom arrays[23–26], have emerged. The KZ ramping technique is particularly well-suited for probing critical phenomena for two complementary reasons. First, quantum simulators allow for versatile dynamical control and site-resolving measurements. Second, dynamical probing bypasses the challenge of adiabatic preparation of a gapless critical state[27], where only a finite coherence time is available on these platforms.

At the intersection of first- and second-order phase transitions, a particular phenomenon known as tricriticality occurs. The tricritical point holds theoretical and practical importance. For instance, spacetime supersymmetry, originally proposed in high-energy physics, can emerge in the low-energy regime of various models[28–33], with one of the most experimentally promising cases being the 1 + 1-dimensional tricritical Ising (TCI) model[34–37]. Tricritical points also play an important role in quantum annealing protocols, where ramping near these points can accelerate optimization processes[38–40]. Furthermore, the proximity to first-order phase transitions raises questions about the validity of standard KZ scaling[41], suggesting that new phenomena may emerge in this context. Despite its importance, no experimentally feasible protocol of tricritical KZ effect has been proposed[42–46].

Here, we propose an experimentally accessible model based on Rydberg atom ladders[47–50], as illustrated in Fig. 1a and b. Figure 1c presents the ground-state phase diagram, controlled by the Rabi frequency and detuning, with the key feature being the tricritical point connecting 1st- and 2nd-order (Ising/Potts) transition lines. The TCI and tricritical Potts (TCP) transitions[51] are realized respectively in the

Institute for Advanced Study, Tsinghua University, Beijing, China. e-mail: chengshu@mail.tsinghua.edu.cn

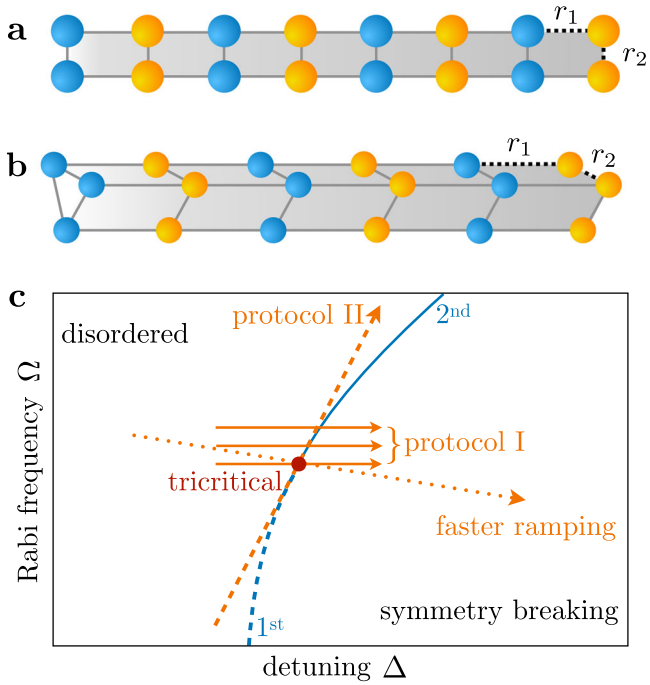

Fig. 1 | Rydberg ladders and Kibble-Zurek protocols. a,**b** Two- and three-leg ladders that exhibit tricritical Ising and Potts points, respectively. Atoms of different colors correspond to different atomic species. The geometry is fixed (i.e., $r_{1,2}$), while the Rabi frequency Ω and detuning Δ can be tuned. **c** The schematic phase diagram and ramping protocols. The solid (dashed) blue line denotes the second (first) order Ising/Potts transition, and a tricritical point lies in between. In Protocol I, we keep Ω fixed and ramp Δ from the disordered phase to the symmetry breaking phase, both across and near the tricritical point. In Protocol II, we consider a tangential ramping direction. The orange dot arrow refers to ramping of higher speeds, where a dynamical analog to Zamolodchikov's *c*-theorem is proposed.

two- and three-leg ladders. From the perspective of renormalization group (RG) theory, these tricritical fixed points are characterized by two symmetry-preserving relevant operators[52,53], introducing rich RG flow behaviors. These additional operators significantly impact the KZ dynamics, in contrast to the more widely studied critical points, which feature only a single symmetry-preserving relevant operator.

Furthermore, since the tricriticality only occurs at a single point in the phase diagram, generically (i.e., with non-vanishing deviation) only intermediate-distance physics is controlled by the tricritical point, with long-distance physics exhibiting more conventional behavior. Indeed, this is a concrete consequence of the celebrated Zamolodchikov's *c*-theorem[54]. Measuring tricritical exponents is therefore challenging in conventional materials, but this very task fits well with the capability of site-resolved imaging in quantum simulators, using dynamical finite-size scaling[7,8,11,19,26,55]. We capitalize on this through the ramping Protocols I and II, as shown in Fig. 1c. Protocol I is of immediate experimental relevance. The conceptual novelty of Protocol II lies in the fact that, throughout the ramping, the system parameters are in the disordered phase, which is beyond the framework relating KZ to domain wall formation. These protocols provide a direct route to measuring distinct tricritical exponents, which can reveal an emergent spacetime supersymmetry constraint in the two-leg case. Moreover, by exploring a much wider range of ramping speeds, the results reveal intriguing crossover behavior from tricriticality to its parent second-order criticality, where a dynamical analog of Zamolodchikov's *c*-theorem is proposed.

Results

Rydberg models and equilibrium phase diagrams

The microscopic models, two- and three-leg Rydberg atom ladders, are modified from a previous model[36]. In both the original and the current models, the system consists of two species of atoms[56–59], assembled in an alternating pattern along the ladder, see Fig. 1a, b. Each atom is modeled by a two-state system, with the ground state $|g\rangle$ and the Rydberg state $|r\rangle$. A laser couples both states and determines the Rabi frequency Ω and detuning Δ through the laser strength and frequency, respectively. The two species are chosen such that Rydberg atoms of the same species repel, while those of different species attract. The Hamiltonian reads

$$H = \sum_i \left(\frac{\Omega}{2} \sigma_i^x - \Delta n_i \right) + \sum_{ij} \frac{C_{XY}}{r_{ij}^6} n_i n_j, \tag{1}$$

where X, Y denote the species of the atoms i and j, and r_{ij} is the interatom distance. $n = |r\rangle\langle r|$ is a projector onto the Rydberg state or, equivalently, the Rydberg number operator. $\sigma_x = |g\rangle\langle r| + \text{h.c.}$ couples the ground state and the Rydberg state. r_2 is chosen to be reasonably small, so that only one atom within a rung can be excited to the Rydberg state due to Rydberg blockade.

In the original model, one fixes r_2 and Ω, and tunes two parameters, namely r_1 and Δ. In the current work, we consider instead tuning Ω and Δ, keeping the geometry fixed throughout, see Fig. 1c. In fact, the phase diagram of the original model has the same structure as in Fig. 1c (with Ω replaced by r_1) thanks to universality (see also the numerical phase diagram in Supplementary Note 1). However, the new setup has the virtue that both Ω and Δ are determined by the laser, and are experimentally readily tuned in a dynamical fashion. In contrast, the lattice geometry is unchangeable during the dynamical evolution. Indeed, the atoms are arranged in a desired geometry by using optical tweezers. During the evolution, with atoms excited to Rydberg states, the tweezers could easily ionize the Rydberg atoms, causing significant atom loss. The upshot is that, in the original model, within each experimental run, one can only move in the horizontal (i.e., detuning) direction in the phase diagram. In the current setup, on the other hand, one is able to move along any path in the phase diagram.

The ladder models have a $\mathbb{Z}_2$ (S_3) symmetry that permutes the two (three) legs. For small Δ, the atoms remain in the ground state, and the system is in the disordered phase. For large Δ, the atoms prefer to be excited to the Rydberg state. However, with Rydberg blockade in action, the best one can do is to excite one of the two (three) legs. This breaks the symmetry to $\varnothing$ (reflective $\mathbb{Z}_2$), and hence we expect the transition to be Ising (three-state Potts) type. For small Ω, the Hamiltonian is dominated by diagonal terms in the Z basis, and the transition tends to be first-order. For large Ω, the quantum fluctuation dominates, and the transition tends to be second-order. In between, TCI (TCP) points emerge, with distinct critical exponents compared to the Ising (Potts) case. All these predictions are corroborated by numerical simulations using density matrix renormalization group (DMRG)[60,61], see Methods for details. With the model and the phase diagram at hand, we next turn to dynamical evolutions. In the main text, we focus on the two-leg ladder. For the three-leg case, results repeat almost verbatim and we postpone them to the Supplementary Note 2.

KZ scalings across and near TCI point

To begin with, we consider ramping from the disordered phase to the ordered phase, similar to the conventional KZ protocol. This is shown in Fig. 1c as Protocol I, where the ramping parameter is given by $g = \Delta - \Delta_{\text{TCI}}$. The ground-state correlation length diverges as $\xi_{\text{GS}} \sim |g|^{-\nu}$, where ν is the critical exponent. Since the correlation length ξ itself has length dimension, i.e., $[\xi] = -1$, the dimension of the ramping parameter is $[g] = 1/\nu$. Next, we define the dynamical process: ramping g with speed s, i.e., $g = st$, with $t = 0$ set as the time passing the phase boundary. By this, one can recover the celebrated KZ scaling of the correlation length, $\xi_{\text{KZ}} \sim s^{-\mu}$, by noting the dimension of speed: $[s] = [g] - [t] = 1/\nu + z \equiv 1/\mu$, where z is the dynamical critical exponent.

https://doi.org/10.1038/s41467-025-65652-9

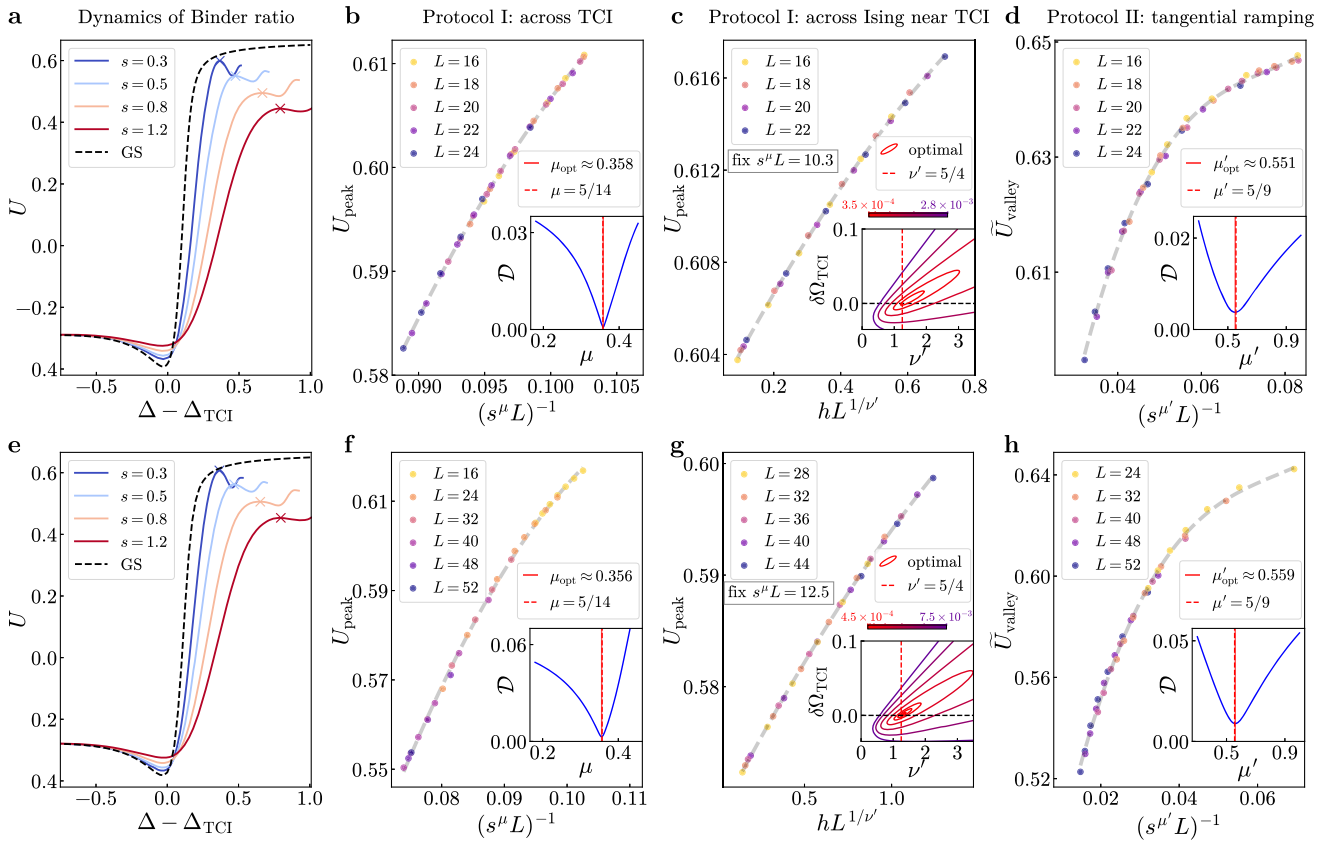

Fig. 2 | KZ scaling of Binder ratio in the TCI case. TEBD simulations using Hamiltonian (1) with $N=2L$ atoms and $1/r^6$ interactions for (**a**–**d**). **a** Binder ratio U as function of $g=\Delta-\Delta_{\rm TCI}\propto t$ for various ramping speed s with $L=16$. The first peak is marked with a cross. The ground state Binder ratio for open boundary conditions (black dashed line) is included for reference. **b** KZ ramping across the TCI point, with data collapse achieved for $s^{\mu}L$. **c** KZ ramping near the TCI point, with data collapse achieved for $hL^{1/\nu'}$. **d** For tangential KZ, we achieve data collapse with $s^{\mu'}L$. In the insets, the data collapse figure of merit $\mathscr{D}$ is plotted against the corresponding critical exponents. **e**–**h** show analogous results using an effective spin-1 model with size L for TEBD simulations. The gray dashed curves represent quadratic fits in (**b**,**c**,**f**,**g**) and cubic fits in (**d**,**h**).

In the quantum simulators we consider, however, the systems are finite-sized, meaning that the correlation length is limited at the critical point rather than diverging. This leads to a deviation from the $\xi_{\rm KZ}\propto s^{-\mu}$ scaling. Fortunately, as in the equilibrium case, finite-size scaling also applies to the KZ mechanism, namely $\xi_{\rm KZ}/L=\mathscr{F}(s^{\mu}L)$[7,8,11,19,26,55], where L is the linear system size (e.g., the length of the ladder in our quasi-1D geometry). However, extracting the length scale $\xi_{\rm KZ}$ from the two-point correlation function introduces ambiguity, and this long-distance feature can easily be affected by noise[26]. Therefore, we choose the Binder ratio U to characterize the dynamics. The main advantages of U are twofold. First, it is dimensionless and does not scale by itself, thus eliminating one additional scaling parameter to be determined. Second, unlike the correlation length, it is a number defined without the need of fitting. Specifically, the time-dependent Binder ratio is defined through the order parameter M as

$$U(t)=1-\frac{\langle\psi(t)|M^4|\psi(t)\rangle}{3\langle\psi(t)|M^2|\psi(t)\rangle^2}. \tag{2}$$

The order parameter is defined as $M=\sum_i n_{ia}-n_{ib}$, where a and b denote the atoms within each rung, and $|\psi(t)\rangle$ is the wavefunction evolved by the Hamiltonian (1) up to time t. This quantity can be readily measured in Rydberg platforms using site-resolved in situ imaging.

Figure 2a shows how the Binder ratio changes over time when ramping across the critical point at different speeds s. We observe that the Binder ratio oscillates rather than directly reaching a plateau, so we need to be cautious when using Binder data to determine scaling laws. The Binder curves at different speeds should show similar behavior due to the scaling invariance of the criticality. We choose the first peak after crossing the critical point ($t>0$) as a reference point for finite-size scaling. This is known as finite-time scaling[62–64], meaning that we do not need to wait for a long time for the quantity to saturate; instead, we use data that is relatively close to the critical point. This is crucial for tricritical physics, as data far from the critical point may not obey tricriticality, as we will see later.

We now discuss our first ramping scheme, Protocol I, which involves ramping across or near the tricritical point, as shown in Fig. 1c. Experimentally, this corresponds to ramping the detuning Δ within a range of fixed Rabi frequency Ω around $\Omega_{\rm TCI}$, with the deviation from the tricritical point parametrized by $h=\Omega-\Omega_{\rm TCI}$. While the tricritical point $\Omega_{\rm TCI}$ can be determined with high precision numerically, achieving this can be tricky experimentally. We will see that without knowing $\Omega_{\rm TCI}$ a priori, using scaling techniques, we can still extract the critical exponents. A side product of our protocol is a method of finding $\Omega_{\rm TCI}$.

From a theoretical perspective, scanning near the tricriticality provides information about two relevant perturbations, resulting in both leading and subleading critical exponents[65–68]. In particular, the leading critical exponent, μ, can be extracted by ramping the parameter g at speed s, following the standard KZ scaling. Simultaneously, the parameter h is associated with a subleading critical exponent, ν', with $[h]=1/\nu'$ (see Methods and Supplementary Fig. 2 for more details). Note that $h^{\nu'}L$ forms a dimensionless combination. These critical exponents can be obtained from conformal field theory (CFT), summarized in Table 1.

Table 1 | The central charge and critical exponents of the universality classes

universality class	c	ν	μ	ν'	μ'
two-leg Ising	1/2	1	1/2	/	/
two-leg TCI	7/10	5/9	5/14	5/4	5/9
three-leg Potts	4/5	5/6	5/11	/	/
three-leg TCP	6/7	7/12	7/19	7/4	7/11

The dynamical exponent z for all cases is 1, due to the emergent Lorentz symmetry.

With these considerations in mind, we propose a dynamical finite-size scaling for Binder peaks near the tricritical point, described by the following equation

$$U_{\text{peak}} = f(s^{\mu}L, h^{\nu'}L), \tag{3}$$

where f is a universal function.

We perform extensive numerical simulations of the dynamical evolution using the time-evolving block decimation (TEBD) algorithm with open boundary conditions[23,26,69–71]. Using the Binder peaks extracted from Fig. 2a for different system sizes L, ramping speeds s, and ramping paths parameterized by h, we verify Eq. (3). In particular, we expect that for exponents μ and ν' that match the universal ones, U_{peak} as a function of $s^{\mu}L$ and $h^{\nu}L$ will exhibit an optimal data collapse. Our numerical results lend full support for this expectation, as shown in the main figures of Fig. 2b, c. Figure 2b corresponds to $h = 0$, i.e., ramping across the tricritical point, and we fix $s^{\mu}L$ and collect data for a window of Ω in Fig. 2c. In the inset of Fig. 2b, we test different values of μ by a figure of merit $\mathscr{D} = \sqrt{\sum_i d_i^2}$, where d_i is the vertical distance between the data point at i and the smooth fitting curve value at the same horizontal value of $s^{\mu}L$. We plot $\mathscr{D}$ as a function of μ, with the minimum corresponding to the optimal data collapse, which agrees closely with the CFT prediction. Next, in the inset of Fig. 2c, we show that we can obtain ν' even without the knowledge of Ω_{TCI} by taking the latter as another optimization parameter. The contour of the figure of merit shows a good agreement with both ν' and the earlier used Ω_{TCI}, and $\delta\Omega_{\text{TCI}}$ in the inset of Fig. 2c represents the difference from the value obtained from DMRG.

Additionally, we perform larger-scale simulations by making certain approximations. Since r_2 is sufficiently small, two atoms in a rung cannot be simultaneously excited to the Rydberg state. Hence, each rung can be recognized as a spin-1 mode (see the Methods section for more details). With such a spin-1 representation, we can simulate much larger system sizes, more than double the original sizes, as shown in Fig. 2f–h. The conclusions drawn from the full $N = 2L$ atom simulations remain unchanged, achieving the same universal scaling behavior.

From the numerical results, we conclude that this protocol provides a highly precise method for probing the leading and subleading critical exponents without the need to prepare critical ground states, bringing the experimental observation of the elusive tricritical point much closer to reality.

Tangential KZ scaling

The two-dimensional phase diagram with a curved phase boundary allows a novel type of KZ scaling, which we dub "tangential" to highlight how the dynamical path touches the phase boundary. The conceptual novelty here lies in the fact that throughout the ramping, one stays exclusively in the disordered phase and never enters the ordered phase, unlike previous KZ protocols. This fact leaves uncertain some heuristic arguments commonly found in the literature, where domain walls or generally topological defects that are only well-defined in the symmetry-breaking phase play a key role. Nevertheless, scaling relations that do not depend on detailed modeling of the dynamics remain valid.

In the tangential ramping, we are effectively ramping the subleading operator, with the leading operator vanishing (see Methods for more details). Hence, the scaling relation is modified to

$$U = f(s^{\mu'}L), \text{ with } \mu' = (z + 1/\nu')^{-1}, \tag{4}$$

which provides a direct probe of the subleading exponent. It is known previously that the Binder ratio works the best in the ordered phase, but scales not as well in the disordered phase[19]. To remedy this, we introduce a disordered Binder ratio $\widetilde{U} = 1 - \frac{1}{3}\langle \widetilde{M}^4 \rangle / \langle \widetilde{M}^2 \rangle^2$. Here, the disorder parameter is defined as

$$\widetilde{M} = \sum_i \prod_{j \geq i} \text{SWAP}_j, \tag{5}$$

where SWAP interchanges the atoms of each rung. The operator can be equivalently written as $\widetilde{M} = \text{SWAP}_1(I_2 + \text{SWAP}_2(\cdots + \text{SWAP}_{L-1}(I_L + \text{SWAP}_L)\cdots))$, which facilitates an efficient matrix-product operator (MPO) calculation. Unlike the ordered Binder ratio, which we choose the peak, the disordered Binder ratio exhibits a valley when tangentially passing through the tricritical point, as shown in Supplementary Note 3. The disordered Binder valleys are collected, and the data collapse is shown in Fig. 2d, which is fully consistent with the scaling relation in Eq. (4).

Dynamical Zamolodchikov's *c*-theorem

Quantum dynamics can be roughly classified by its characteristic time scale, with adiabaticity and quenching as the two opposite limits. In the case of KZ, a natural parameter is the ramping speed s, and s is generally assumed to be small so that the physics is well controlled by the critical point. In previous discussions, this is also the regime we focused on. Now we go slightly beyond and focus on intermediate-speed ramping.

Heuristically, upon inspecting the phase diagram in Fig. 1c with a 0d tricritical point and a 1d critical line, we expect only the neighboring region of the tricritical point to be controlled by its universal property, and as one moves far away, the Ising/Potts criticality takes over. The argument can be made more precise by examining the RG flow around the tricritical point, see Fig. 3a. One sees that far away from the tricritical point, the RG flow generically takes a detour near the critical line, thus inheriting criticality from the latter[72,73].

Returning to dynamics, it follows that the tricritical exponents can only be observed with sufficiently slow ramping. This is evident in Fig. 3b, where the upper-right corner of the figure shows a good data collapse when the horizontal axis is scaled by the tricritical exponent μ_{TCI}. For faster ramping speeds, data for different system sizes is spread out. However, if we rescale the horizontal axis by the critical exponent μ_{Ising}, as shown in Fig. 3c, the data collapse is restored in the fast-ramping regime. This indicates that in this regime, the emergent TCI is not observed, but the original Ising criticality manifests instead. This result holds generally for different ramping directions through the tricritical point. Specifically, by choosing a direction in which the tricriticality extends the furthest in the ground state (Supplementary Note 4), one might expect that only TCI would be observed in this regime. Nevertheless, we still observe Ising criticality dominating the dynamics. The appearance of two distinct critical exponents across different ramping speed ranges is a generic feature that reflects this rich RG structure, as we also demonstrate for the three-leg case (see Supplementary Note 2).

These results are reminiscent of the celebrated Zamolodchikov's *c*-theorem. The theorem states that along an RG flow the central charge c has to decrease. This physics is again well represented by the case of

https://doi.org/10.1038/s41467-025-65652-9

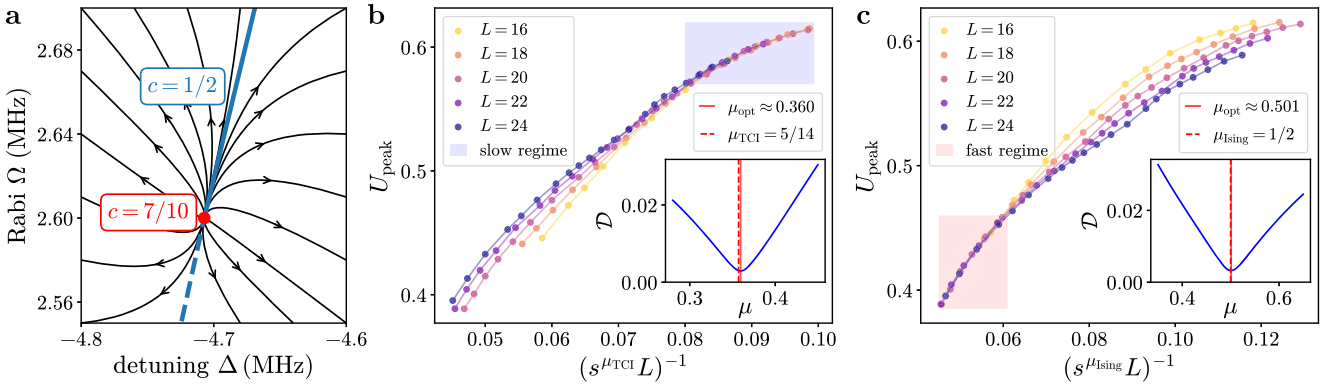

Fig. 3 | RG perspective of KZ in the TCI case. a RG flow (black lines) near the TCI. The blue line indicates the numerical phase boundary determined by Binder ratio and central charge (see Methods). **b**,**c** Ramping with a broad range of ramping speed s. Both figures are plotted with the same data but with different scalings of s. For slower ramping (upper right region in (**b**)), the TCI critical exponent allow the best data collapse. For faster ramping (lower left region in (**c**)), the Ising critical exponent allow the best data collapse.

tricritical points in the ground state, where two different criticalities come into play, and is best illustrated by the RG flow in Fig. 3a. Although the KZ protocols do not directly measure the central charge, our observed crossover behavior still largely conforms to the same phenomenology, namely a flow from tricriticality (high c) to the Ising/Potts criticality (low c).

Discussion

In this work, we systematically investigate the KZ scaling near tricritical points, using two- and three-leg Rydberg ladders. Through both conventional and tangential ramping protocols near the tricritical point, we accurately determine the critical exponents associated with the two relevant operators, in close agreement with their CFT predictions at the exact tricriticality. Additionally, we uncover a dynamical analog of Zamolodchikov's c-theorem in an intermediate-speed ramping regime.

We anticipate an imminent experimental realization of our proposals, particularly for the two-leg model, which only requires a planar geometry and harbors TCI criticality. Looking forward, the TCI is closely related to spacetime supersymmetry—a long-sought concept in theoretical physics. In our setup, the critical exponents ν and ν' correspond to the bosonic sector of the two lowest weight symmetry-preserving fields, ϵ and ϵ'. These fields exhibit power-law correlations, $\langle \epsilon_i \epsilon_j \rangle \sim |i-j|^{-2\Delta_\epsilon}$, with $\Delta_\epsilon = 2 - 1/\nu$ (and similarly for ϵ', giving $\Delta_{\epsilon'}$). Notably, $\Delta_{\epsilon'} - \Delta_\epsilon = 1/\nu - 1/\nu' = 1$. This relationship is no coincidence: the fermionic mode ψ is linked to these fields through the supersymmetry generator, resulting in the relation $\Delta_\psi = \Delta_\epsilon + 1/2 = \Delta_{\epsilon'} - 1/2$, illustrating the structure of fermion bridging the two bosons. Hence, our protocol offers an effective method of corroborating this nontrivial ramification of emergent supersymmetry. On the other hand, directly measuring the corresponding fermion ψ dynamically remains an open question, as it would likely require ramping fermionic operators[36,74]. This introduces an interesting direction for future research, which we intend to explore further.

Note added: In a recent post[75], the authors also investigate the KZ mechanism at a supersymmetric tricritical point with two relevant directions. Although their model differs from ours, the same universality emerges, leading to overlapping and mutually corroborating findings.

Methods

Ground state phase diagrams

We describe the method used to obtain the ground state phase diagrams for the two- and three-leg ladders. In both cases, we employ DMRG to compute the ground state $|\psi\rangle$.

For each Rabi frequency Ω, we sweep the detuning Δ to calculate the Binder ratio of the ground state under periodic boundary conditions (PBC), $U_{\text{GS}}(L,\Omega,\Delta) = 1 - \frac{1}{3}\langle\psi|M^4|\psi\rangle / \langle\psi|M^2|\psi\rangle^2$. For different system sizes L, the Binder curve U_{GS} versus Δ crosses at a single point, which is used to determine the transition point. By collecting the transition detuning values along with their corresponding Rabi frequencies, we obtain the phase boundary.

Next, we identify the tricritical point by calculating the central charge c along the phase boundary. The maximum value of c identifies the tricritical point[36]. Specifically, we calculate the entanglement entropy along the phase boundary. The entanglement entropy $S(l)$ of a subsystem with length l is defined as $S(l) = -\text{Tr}\rho(l)\log\rho(l)$, where $\rho(l) = \text{Tr}_{L\setminus l}|\psi\rangle\langle\psi|$ is the reduced density matrix obtained from the ground state $|\psi\rangle$ calculated under PBC. The central charge of the state is then obtained by fitting the entanglement entropy to[76,77]

$$S(l) = \frac{c}{3}\log\left[\sin\left(\frac{\pi l}{L}\right)\right] + \text{const}. \tag{6}$$

For the two-leg model, we use cesium 70S (a-type) and sodium 69S (b-type) as the two species of atoms in the main text. The interactions between atoms are van der Waals C/r^6, with interaction constants $(C_{\text{aa}}, C_{\text{bb}}, C_{\text{ab}}) = (650, 1570, -614)\,\text{GHz}\,\mu\text{m}^6$. The Rydberg blockade is manifest with $r_2 = 5\,\mu$m. Then $r_1 = 7\,\mu$m sets the attractive energy scale to 5.2 MHz. This energy scale controls the position of the tricritical point Ω_{TCI} and Δ_{TCI}, allowing one to tune it to a desired value in experiments by adjusting r_1. With these parameters, we plot how c changes along the phase boundary characterized by Ω, near the tricritical regime, as shown in Supplementary Fig. 2a. The central charge peaks at $\Omega_{\text{TCI}} \approx 2.6$ MHz with $c = 7/10$, and gradually decreases to 1/2 in the direction toward the standard second-order line. The tangential scaling ν' is explicitly demonstrated in the inset, through proper data collapse with the horizontal axis $hL^{1/\nu'}$. The numerical phase diagrams are presented in Supplementary Note 1 and share the same features as Fig. 1c in the main text.

Besides the full-range van der Waals calculation mentioned above, we also performed finite-range interaction calculations (i.e., truncating longer-range interactions). In the latter case, we include interactions up to: ○○●○○ / ○○○○○, where ● represents the reference atom and ○ represents atoms whose interactions with the reference atom are included. We find no differences between the full-range and such finite-range DMRG results. The reason for checking finite-range interactions is that in dynamical simulations, including all-range interactions makes Trotter decomposition very challenging. Hence, in the dynamics calculations, as detailed in the following section, we include only this finite range of interactions.

For the three-leg ladder case, we also performed the same calculation with the same parameters of cesium 70S and sodium 69S as used in the two-leg case, by simply adding one more atom to each rung, as shown in Fig. 1b. The central charge result is similar to its two-leg cousin, except that the numerical values of the central charge and critical exponents follow those of Potts and tricritical Potts, see Supplementary Fig. 2b. However, it is quite heavy to perform dynamical evolution with the full setup. Hence, to demonstrate the universality feature of the physics, we also propose an effective model, as detailed in the following section. The same universality is found, with the phase diagram presented in Supplementary Note 1.

The effective model for the two-leg ladder

Here, we present an effective description of the two-leg ladder when the blockade condition is well satisfied. In each rung, two spin-1/2 atoms form a Hilbert space of four states. If both atoms cannot be simultaneously excited due to the blockade, then only three states remain accessible, and each rung can be effectively described as a spin-1 mode. To be more specific, we label the atoms on the upper rung as $i = 1, 3, 5, \ldots, 2L-1$ and the lower rung atoms as $j = 2, 4, 6, \ldots, 2L$. Each rung is labeled by $I = 1, 2, 3, \ldots, L$, which also labels the corresponding spin-1. In this representation, the Hamiltonian (1) can be written in terms of S^x and S^z operators, with the following correspondence:

$$\begin{aligned}
\Omega(\sigma_i^x + \sigma_j^x) &\leftrightarrow \sqrt{2}\Omega S_I^x \\
\Delta(n_i + n_j) &\leftrightarrow \Delta S_I^z \\
V_1^{ab}(n_i n_{i+1} + n_j n_{j+1}) &\leftrightarrow \frac{V_1^{ab} - V_2^{ab}}{2} S_I^z S_{I+1}^z \\
V_2^{ab}(n_i n_{j+1} + n_{i+1} n_j) &\leftrightarrow \frac{V_1^{ab} + V_2^{ab}}{2} (S_I^z)^2 (S_{I+1}^z)^2
\end{aligned} \tag{7}$$

where the attractive interaction between dual-species atoms is given by $V_1^{ab} = C_{ab}/r_1^6$ (upper-upper/lower-lower interaction) and $V_2^{ab} = C_{ab}/(r_1^2 + r_2^2)^3$ (upper-lower/lower-upper interaction). Longer-range interactions between S_I^z and S_{I+2}^z can also be included, with repulsive interaction strengths $V_1^{aa} = C_{aa}/(2r_1)^6$ and $V_2^{aa} = C_{aa}/((2r_1)^2 + r_2^2)^3$, and similar expressions for V_1^{bb} and V_2^{bb}.

The same universality is observed in the ground state phase diagram, with the non-universal feature that the position of the tricritical point is shifted by approximately 5% when only attractive effects are included. When longer-range repulsive interactions are also included, the position of the tricritical point shifts by approximately 0.6% compared to the full range spin-1/2 model.

The effective model for the three-leg ladder

The effective Hamiltonian for the three-leg ladder reads

$$H = \sum_i \frac{\Omega}{2} X_i - \Delta n_i - J n_i n_{i+1}. \tag{8}$$

In this effective model, by enforcing Rydberg blockade, each site has four states $|0\rangle, |a\rangle, |b\rangle$ and $|c\rangle$, corresponding to all atoms in the ground state or one of the atoms on a rung excited to the Rydberg state, respectively. $X = \sum_{\alpha=a,b,c} |\alpha\rangle\langle 0| + \text{h.c.}$ couples the ground state and the Rydberg state as usual, and $n = \sum_{\alpha=a,b,c} |\alpha\rangle\langle\alpha|$ projects to the Rydberg states. Inter-rung attractive interactions are encompassed in a coupling constant J, which we set to 1 as the energy scale.

To properly work with the three-leg ladder, we need to redefine several physical quantities. The order parameter is defined by

$$M_3 = \sum_i n_{ia} + e^{2\pi i/3} n_{ib} + e^{4\pi i/3} n_{ic}, \tag{9}$$

and the disorder operator reads

$$\widetilde{M}_3 = \sum_i \prod_{j \geq i} \text{CYCL}_j, \tag{10}$$

where $\text{CYCL} = |0\rangle\langle 0| + |b\rangle\langle a| + |c\rangle\langle b| + |a\rangle\langle c|$ permutes the atoms along the rungs. A numerics-friendly version is $\widetilde{M}_3 = \text{CYCL}_1(I_2 + \text{CYCL}_2(\cdots + \text{CYCL}_{L-1}(I_L + \text{CYCL}_L)\cdots))$. The Binder ratio can then be defined in the same way as described in the main text.

Numerical simulation of KZ dynamics

We employ the TEBD algorithm to simulate the KZ dynamics. We include finite-range interactions and use Trotter decomposition for the unitary evolution with open boundary conditions. During the ramping process, the time step is fixed at Δt. To ensure the convergence of our results, we test different values of $\Delta t = 0.0004, 0.0002, 0.0001\,\mu s$, always obtaining consistent results. All ramping speeds in the main text are given in units of MHz/μs. The singular value decomposition truncation cutoff of 5×10^{-12} is used. With this approach, the time-dependent wavefunction $|\psi(t)\rangle$ is obtained, and various physical operators can be measured from this wavefunction to extract the quantities discussed in the main text.

For the two-leg case, as the DMRG results suggest, finite-range truncation of the C/r^6 interactions in Hamiltonian (1) still exhibits proper tricriticality. In the dynamical simulation, when implementing the Trotter decomposition, interactions are included for every group of six atoms. For example, the ● atom participates in three different groupings: ○○●/○○○, ○●○/○○○, ●○○/○○○. Boundary atoms are handled appropriately under open boundary conditions by adjusting the grouping scheme near the edges, following approaches similar to refs. 23,26. These simulations produce the results shown in Fig. 2a–d. Additionally, we employ the spin-1 representation [cf. Eqs. (7)] for TEBD simulations. This approach reduces the dimension of the local Hilbert space, making dynamical simulations feasible for much larger system sizes, as demonstrated in Fig. 2e–h. Importantly, the same universal dynamical scalings are uncovered in both methods.

For the three-leg case, we use Hamiltonian (8) for TEBD simulations, and results are summarized in Supplementary Note 2.

Critical exponents and scaling dimensions

In the main text, we identified two critical exponents ν and ν' near the tricriticality. In the CFT language, these exponents correspond to two symmetry-preserving relevant conformal fields, ϵ and ϵ', in TCI/Potts CFT, with scaling dimensions Δ_ϵ and $\Delta_{\epsilon'}$, respectively.

The ϵ field is very similar to its counterpart at the parent critical line. It drives the system between disordered and ordered phases. For a shifted parameter g, the field couples to it with an additional action term compared to the critical point value: $S = \int dx\, d\tau\, g \cdot \epsilon$. Near criticality, scaling invariance is still preserved and action is unchanged under the following scaling transformations with ratio b:

$$x \to b^{-1}x,\ \tau \to b^{-z}\tau,\ g \to b^{1/\nu} g,\ \epsilon \to b^{\Delta_\epsilon}\epsilon \tag{11}$$

This immediately gives the relation between the critical exponents that can be measured in experiments and the scaling dimension of the coupled conformal field: $\Delta_\epsilon + 1/\nu = 1 + z$ [cf. Table 1 and Supplementary Table I].

The ϵ field, as the most relevant operator, is responsible for the spontaneous symmetry breaking. However, in the phase diagram spanned by two parameters, there is a direction that does not lead to either phase—namely, the direction parallel to the local phase boundary. In this direction, the perturbation involving ϵ is completely canceled, and the subleading field ϵ' takes charge. We denote the angle of the phase boundary relative to the detuning direction as θ, and the

deviation in this direction from the tricritical point as $h_{\parallel}$. This angle θ can be determined by expanding lattice operators in terms of conformal fields, as illustrated in the next subsection. $h_{\parallel}$ refers to the strength of deviation from the tricritical point, with the equilibrium critical exponent defined as ν'. Since $h_{\parallel}$ couples to ϵ', which contributes most significantly to the action, following the same argument gives $\Delta_{\epsilon'} + 1/\nu' = 1 + z$. In the main text, we define $h = \Omega - \Omega_{\mathrm{TCI}}$ to control the deviation from the tricritical point, which has the relation $h = h_{\parallel} \sin(\theta)$. We use the dimension $[h] = 1/\nu'$ in this sense, as verified by the central charge scaling along the phase boundary shown in the insets of Supplementary Fig. 2.

With these equilibrium features near the tricritical point, we therefore propose a "tangential ramping" protocol that tangentially approaches the tricritical point. In this direction, before reaching the near-tricritical regime, the energy gap remains finite. Near the tricritical point, the KZ mechanism becomes relevant due to the gapless nature, with the scaling entirely controlled by ϵ' and thus enabling measurement of μ'.

Expansion of lattice operators by conformal fields

In this section, we explain how we obtain the RG flow at the tricritical point shown in Fig. 3a. We relate lattice operators σ^x, n [cf. Eq. (1)] to conformal fields. From symmetry considerations, we have

$$\begin{aligned} \sigma^x &= \langle \sigma^x \rangle + a_1 \epsilon + a_2 \epsilon' + \ldots \\ n &= \langle n \rangle + b_1 \epsilon + b_2 \epsilon' + \ldots \end{aligned} \tag{12}$$

We note that σ^x and n are coupled to Ω and Δ, respectively. Once we determine these coefficients, and hence the relative strength between ϵ and ϵ', we can establish (i) the direction of the phase boundary (where the ϵ component vanishes) and (ii) the generic RG flow trajectory in the phase diagram with parameters Ω and Δ. We explain how to extract these coefficients numerically below.

The main analytical tool we use is the state–operator correspondence in CFT. Roughly speaking, this relates the energy eigenstates of a microscopic model to the primary fields of the field theory. Two important consequences follow. First, the energies of the lowest eigenstates are given by $E_\phi = \Delta_\phi + n$, where Δ_ϕ is the conformal dimension of the field ϕ and n labels the descendant level. Here we have shifted and rescaled the energy spectrum so that the ground state has zero energy and descendant states have unit energy intervals. We can thus identify the particular states $|\epsilon\rangle$, $|\epsilon'\rangle$, see Supplementary Fig. 3. Second, we have the matrix element $\langle \phi | \phi | 0 \rangle = (2\pi/L)^{\Delta_\phi}$. Combined with the expansion, Eq. (12), we can extract the four coefficients of interest. The conformal dimensions and the numerical results are collected in Supplementary Table I. This is the data we used to plot the RG flow in Fig. 3a. We also mention that the densest direction of the RG trajectory lines coincides with the DMRG phase boundary calculation (blue line, obtained using the Binder ratio), showing good agreement in determining the tangential direction.

Data availability

The data generated in this study have been deposited in the Zenodo database under identifier https://doi.org/10.5281/zenodo.17385416.

Code availability

The numerical codes used in this study are available from the corresponding author upon request.

References

1. Kibble, T. W. Topology of cosmic domains and strings. *J. Phys. Math. Gen.* **9**, 1387–1389 (1976).
2. Zurek, W. H. Cosmological experiments in superfluid helium? *Nature* **317**, 505–508 (1985).
3. Zurek, W. H., Dorner, U. & Zoller, P. Dynamics of a quantum phase transition. *Phys. Rev. Lett.* **95**, 105701 (2005).
4. Dziarmaga, J. Dynamics of a quantum phase transition: exact solution of the quantum ising model. *Phys. Rev. Lett.* **95**, 245701 (2005).
5. Polkovnikov, A. Universal adiabatic dynamics in the vicinity of a quantum critical point. *Phys. Rev. B* **72**, 161201 (2005).
6. Polkovnikov, A., Sengupta, K., Silva, A. & Vengalattore, M. Colloquium: nonequilibrium dynamics of closed interacting quantum systems. *Rev. Mod. Phys.* **83**, 863–883 (2011).
7. De Grandi, C., Polkovnikov, A. & Sandvik, A. Universal nonequilibrium quantum dynamics in imaginary time. *Phys. Rev. B* **84**, 224303 (2011).
8. Kolodrubetz, M., Clark, B. K. & Huse, D. A. Nonequilibrium dynamic critical scaling of the quantum ising chain. *Phys. Rev. Lett.* **109**, 015701 (2012).
9. Chandran, A., Erez, A., Gubser, S. S. & Sondhi, S. L. Kibble-Zurek problem: universality and the scaling limit. *Phys. Rev. B* **86**, 064304 (2012).
10. del Campo, A. & Zurek, W. H. Universality of phase transition dynamics: topological defects from symmetry breaking. *Int. J. Mod. Phys. A* **29**, 1430018 (2014).
11. Rossini, D. & Vicari, E. Coherent and dissipative dynamics at quantum phase transitions. *Phys. Rep.* **936**, 1–110 (2021).
12. Bermudez, A., Patanè, D., Amico, L. & Martin-Delgado, M. A. Topology-induced anomalous defect production by crossing a quantum critical point. *Phys. Rev. Lett.* **102**, 135702 (2009).
13. Bermudez, A., Amico, L. & Martin-Delgado, M. Dynamical delocalization of Majorana edge states by sweeping across a quantum critical point. *New J. Phys.* **12**, 055014 (2010).
14. Ulčakar, L., Mravlje, J. & Rejec, T. Kibble-Zurek behavior in disordered Chern insulators. *Phys. Rev. Lett.* **125**, 216601 (2020).
15. Yuan, H., Zhang, J., Chen, S. & Nie, X. Kibble-Zurek behavior in a topological phase transition with a quadratic band crossing. *Phys. Rev. B* **110**, 165130 (2024).
16. Shu, Y.-R., Jian, S.-K., Sandvik, A. W. & Yin, S. Equilibration of topological defects near the deconfined quantum multicritical point. *Nat. Commun.* **16**, 3402 (2025).
17. Deng, M., Sun, Z. & Li, F. Defect production across higher-order phase transitions beyond Kibble-Zurek scaling. *Phys. Rev. Lett.* **134**, 010409 (2025).
18. King, A. D. et al. Coherent quantum annealing in a programmable 2000 qubit Ising chain. *Nat. Phys.* **18**, 1324–1328 (2022).
19. King, A. D. et al. Quantum critical dynamics in a 5000-qubit programmable spin glass. *Nature* **617**, 61–66 (2023).
20. Ulm, S. et al. Observation of the Kibble–Zurek scaling law for defect formation in ion crystals. *Nat. Commun.* **4**, 2290 (2013).
21. Pyka, K. et al. Topological defect formation and spontaneous symmetry breaking in ion Coulomb crystals. *Nat. Commun.* **4**, 2291 (2013).
22. Li, B.-W. et al. Probing critical behavior of long-range transverse-field Ising model through quantum Kibble-Zurek mechanism. *PRX Quantum* **4**, 010302 (2023).
23. Keesling, A. et al. Quantum Kibble–Zurek mechanism and critical dynamics on a programmable Rydberg simulator. *Nature* **568**, 207–211 (2019).
24. Ebadi, S. et al. Quantum phases of matter on a 256-atom programmable quantum simulator. *Nature* **595**, 227–232 (2021).
25. Manovitz, T. et al. Quantum coarsening and collective dynamics on a programmable simulator. *Nature* **638**, 86–92 (2025).
26. Zhang, T. et al. Observation of near-critical Kibble-Zurek scaling in Rydberg atom arrays. *Phys. Rev. Lett.* **135**, 093403 (2025).
27. Fang, F. et al. Probing critical phenomena in open quantum systems using atom arrays. arXiv:2402.15376.

28. Grover, T., Sheng, D. & Vishwanath, A. Emergent space-time supersymmetry at the boundary of a topological phase. *Science* **344**, 280–283 (2014).
29. Jian, S.-K., Jiang, Y.-F. & Yao, H. Emergent spacetime supersymmetry in 3D Weyl semimetals and 2D dirac semimetals. *Phys. Rev. Lett.* **114**, 237001 (2015).
30. Jian, S.-K., Lin, C.-H., Maciejko, J. & Yao, H. Emergence of supersymmetric quantum electrodynamics. *Phys. Rev. Lett.* **118**, 166802 (2017).
31. Li, Z.-X., Vaezi, A., Mendl, C. B. & Yao, H. Numerical observation of emergent spacetime supersymmetry at quantum criticality. *Sci. Adv.* **4**, eaau1463 (2018).
32. Li, C., Ebisu, H., Sahoo, S., Oreg, Y. & Franz, M. Coupled wire construction of a topological phase with chiral tricritical Ising edge modes. *Phys. Rev. B* **102**, 165123 (2020).
33. Zeng, Z., Yu, Y.-K., Li, Z.-X. & Yin, S. Nonequilibrium critical dynamics with emergent supersymmetry. *Phys. Rev. B* **112**, L060301 (2025).
34. Friedan, D., Qiu, Z. & Shenker, S. Superconformal invariance in two dimensions and the tricritical Ising model. *Phys. Lett. B* **151**, 37–43 (1985).
35. Zamolodchikov, A. B. Conformal symmetry and multicritical points in two-dimensional quantum field theory. *Sov. J. Nucl. Phys.* **44**, 529 (1986).
36. Li, C. et al. Uncovering emergent spacetime supersymmetry with Rydberg atom arrays. *Phys. Rev. Lett.* **133**, 223401 (2024).
37. Cheng, Y. & Liu, S. Unveiling spacetime supersymmetry in the truncated lattice Schwinger model. *Phys. Rev. B*. https://doi.org/10.1103/qwrr-9k78 (2025).
38. Wang, H., Yeh, H.-C. & Kamenev, A. Many-body localization enables iterative quantum optimization. *Nat. Commun.* **13**, 5503 (2022).
39. Zhang, H., Boothby, K. & Kamenev, A. Cyclic quantum annealing: searching for deep low-energy states in 5000-qubit spin glass. *Sci. Rep.* **14**, 30784 (2024).
40. Zhang, H. & Kamenev, A. Computational complexity of three-dimensional Ising spin glass: lessons from D-wave annealer. *Phys. Rev. Res.* **7**, 033098 (2025).
41. Suzuki, F. & Zurek, W. H. Topological defect formation in a phase transition with tunable order. *Phys. Rev. Lett.* **132**, 241601 (2024).
42. Mukherjee, V., Divakaran, U., Dutta, A. & Sen, D. Quenching dynamics of a quantum *XY* spin-$\frac{1}{2}$ chain in a transverse field. *Phys. Rev. B* **76**, 174303 (2007).
43. Divakaran, U., Mukherjee, V., Dutta, A. & Sen, D. Defect production due to quenching through a multicritical point. *J. Stat. Mech. Theor. Exper.* **2009**, P02007 (2009).
44. Deng, S., Ortiz, G. & Viola, L. Anomalous nonergodic scaling in adiabatic multicritical quantum quenches. *Phys. Rev. B* **80**, 241109 (2009).
45. Mukherjee, V. & Dutta, A. Adiabatic multicritical quantum quenches: continuously varying exponents depending on the direction of quenching. *Europhys. Lett.* **92**, 37004 (2010).
46. Patra, A., Mukherjee, V. & Dutta, A. Non-equilibrium dynamics near a quantum multicritical point. *J. Phys. Conf. Ser.* **297**, 012008 (2011).
47. Sarkar, M., Pal, M., Sen, A. & Sengupta, K. Quantum order-by-disorder induced phase transition in Rydberg ladders with staggered detuning. *SciPost Phys.* **14**, 004 (2023).
48. Zhang, J. et al. Probing quantum floating phases in Rydberg atom arrays. *Nat. Commun.* **16**, 712 (2025).
49. Kerschbaumer, A., Ljubotina, M., Serbyn, M. & Desaules, J.-Y. Quantum many-body scars beyond the PXP model in Rydberg simulators. *Phys. Rev. Lett.* **134**, 160401 (2025).
50. Soto-Garcia, J. & Chepiga, N. Numerical investigation of quantum phases and phase transitions in a two-leg ladder of Rydberg atoms. *Phys. Rev. Res.* **7**, 013215 (2025).
51. Nienhuis, B., Berker, A. N., Riedel, E. K. & Schick, M. First- and second-order phase transitions in Potts models: renormalization-group solution. *Phys. Rev. Lett.* **43**, 737–740 (1979).
52. Di Francesco, P., Mathieu, P. & Sénéchal, D. *Conformal Field Theory* (Springer-Verlag, 1997).
53. Cardy, J.*Scaling and Renormalization in Statistical Physics* (Cambridge University Press, 1996).
54. Zamolodchikov, A. B. Irreversibility of the flux of the renormalization group in a 2D field theory. *JETP Lett.* **43**, 730–732 (1986).
55. Liu, C.-W., Polkovnikov, A. & Sandvik, A. W. Dynamic scaling at classical phase transitions approached through nonequilibrium quenching. *Phys. Rev. B* **89**, 054307 (2014).
56. Zeng, Y. et al. Entangling two individual atoms of different isotopes via Rydberg blockade. *Phys. Rev. Lett.* **119**, 160502 (2017).
57. Sheng, C. et al. Defect-free arbitrary-geometry assembly of mixed-species atom arrays. *Phys. Rev. Lett.* **128**, 083202 (2022).
58. Singh, K., Anand, S., Pocklington, A., Kemp, J. T. & Bernien, H. Dual-element, two-dimensional atom array with continuous-mode operation. *Phys. Rev. X* **12**, 011040 (2022).
59. Anand, S. et al. A dual-species Rydberg array. *Nat. Phys.* **20**, 1744–1750 (2024).
60. White, S. R. Density matrix formulation for quantum renormalization groups. *Phys. Rev. Lett.* **69**, 2863–2866 (1992).
61. Schollwöck, U. The density-matrix renormalization group in the age of matrix product states. *Ann. Phys.* **326**, 96–192 (2011).
62. Gong, S., Zhong, F., Huang, X. & Fan, S. Finite-time scaling via linear driving. *New J. Phys.* **12**, 043036 (2010).
63. Huang, Y., Yin, S., Feng, B. & Zhong, F. Kibble-Zurek mechanism and finite-time scaling. *Phys. Rev. B* **90**, 134108 (2014).
64. Shu, Y.-R., Yang, L.-Y. & Yin, S. Finite-time scaling with two characteristic time scales: driven critical dynamics with emergent symmetry. arXiv:2503.16796.
65. Wilding, N. B. & Nielaba, P. Tricritical universality in a two-dimensional spin fluid. *Phys. Rev. E* **53**, 926–934 (1996).
66. Kwak, W., Jeong, J., Lee, J. & Kim, D.-H. First-order phase transition and tricritical scaling behavior of the Blume-Capel model: a Wang-Landau sampling approach. *Phys. Rev. E* **92**, 022134 (2015).
67. Mathey, S. & Diehl, S. Activating critical exponent spectra with a slow drive. *Phys. Rev. Res.* **2**, 013150 (2020).
68. Ladewig, B., Mathey, S. & Diehl, S. Kibble-Zurek mechanism from different angles: the transverse XY model and subleading scalings. *Phys. Rev. B* **102**, 104306 (2020).
69. Vidal, G. Efficient classical simulation of slightly entangled quantum computations. *Phys. Rev. Lett.* **91**, 147902 (2003).
70. Verstraete, F., García-Ripoll, J. J. & Cirac, J. I. Matrix product density operators: simulation of finite-temperature and dissipative systems. *Phys. Rev. Lett.* **93**, 207204 (2004).
71. Garcia, J. S. & Chepiga, N. The quantum Kibble-Zurek mechanism: the role of boundary conditions, endpoints and kink types. arXiv:2412.20186.
72. Wang, H., Li, C., Li, X., Gu, Y. & Liu, S. Lattice defects in Rydberg atom arrays. *Phys. Rev. B*. https://doi.org/10.1103/zf2q-gxr1.
73. Li, X., Zhou, S., Chen, X., Li, C. & Wang, H. On random displacements in critical Rydberg atom arrays. arXiv:2508.05381.
74. Bravyi, S. B. & Kitaev, A. Y. Fermionic quantum computation. *Ann. Phys.* **298**, 210–226 (2002).
75. Wang, T.-L., Jiang, Y.-F. & Yin, S. Driven critical dynamics in tricitical point. *Chinese Phys. Lett.* https://doi.org/10.1088/0256-307X/42/11/110001.
76. Vidal, G., Latorre, J. I., Rico, E. & Kitaev, A. Entanglement in quantum critical phenomena. *Phys. Rev. Lett.* **90**, 227902 (2003).
77. Calabrese, P. & Cardy, J. Entanglement entropy and quantum field theory. *J. Stat. Mech. Theor. Exp.* **2004**, P06002 (2004).

78. Fishman, M., White, S. R. & Stoudenmire, E. M. The ITensor software library for tensor network calculations. *SciPost Phys. Codebases* 4 (2022).

Acknowledgements

We are grateful to Hui Zhai for collaboration on related projects and stimulating ideas. We thank Wenjun Zhang for helpful discussions on the experimental details. We thank Shuai Yin for reading our manuscript and providing valuable feedback. This work is supported by National Natural Science Foundation of China under Grant No. 12504307 (C.L.). C.L. is also supported by Tsinghua University Dushi program. H.W. is supported by China Postdoctoral Science Foundation under Grant No. 2024M751609 and Postdoctoral Fellowship Program of CPSF under Grant No. GZC20231364. The DMRG and TEBD calculations are performed using the ITensor library[78].

Author contributions

H.W., X.L., and C.L. contributed to developing the theory. H.W. performed the numerical simulations. All authors analyzed the data and wrote the manuscript.

Competing interests

The authors declare no competing interests.

Additional information

Supplementary information The online version contains supplementary material available at https://doi.org/10.1038/s41467-025-65652-9.

Correspondence and requests for materials should be addressed to Chengshu Li.

Peer review information *Nature Communications* thanks the anonymous reviewers for their contribution to the peer review of this work. A peer review file is available.

Reprints and permissions information is available at http://www.nature.com/reprints

Publisher's note Springer Nature remains neutral with regard to jurisdictional claims in published maps and institutional affiliations.

Open Access This article is licensed under a Creative Commons Attribution-NonCommercial-NoDerivatives 4.0 International License, which permits any non-commercial use, sharing, distribution and reproduction in any medium or format, as long as you give appropriate credit to the original author(s) and the source, provide a link to the Creative Commons licence, and indicate if you modified the licensed material. You do not have permission under this licence to share adapted material derived from this article or parts of it. The images or other third party material in this article are included in the article's Creative Commons licence, unless indicated otherwise in a credit line to the material. If material is not included in the article's Creative Commons licence and your intended use is not permitted by statutory regulation or exceeds the permitted use, you will need to obtain permission directly from the copyright holder. To view a copy of this licence, visit http://creativecommons.org/licenses/by-nc-nd/4.0/.

© The Author(s) 2025